



Multi-perspective Adaptive Iteration Network for Metal Artifact Reduction

Haiyang Mao¹, Yanyang Wang¹, Hengyong Yu², Weiwen Wu^{1(✉)},
and Jianjia Zhang^{1(✉)}

¹ School of Biomedical Engineering, Shenzhen Campus of Sun Yat-sen University,
Shenzhen 518107, China

{wuweiw7,zhangjj225}@mail.sysu.edu.cn

² University of Massachusetts Lowell, Lowell, MA 01854, USA

Abstract. Metal artifact reduction (MAR) is important to alleviate the impacts of metal implants on clinical diagnosis with CT images. However, enhancing the quality of metal-corrupted image remains a challenge. Although the deep learning-based MAR methods have achieved impressive success, their interpretability and generalizability need further improvement. It is found that metal artifacts mainly concentrate in high frequency, and their distributions in the wavelet domain are significantly different from those in the image domain. Decomposing metal artifacts into different frequency bands is conducive for us to characterize them. Based on these observations, a model is constructed with dual-domain constraints to encode artifacts by utilizing wavelet transform. To facilitate the optimization of the model and improve its interpretability, a novel multi-perspective adaptive iteration network (MAIN) is proposed. Our MAIN is constructed under the guidance of the proximal gradient technique. Moreover, with the usage of the adaptive wavelet module, the network gains better generalization performance. Compared with the representative state-of-the-art deep learning-based MAR methods, the results show that our MAIN significantly outperforms other methods on both of a synthetic and a clinical datasets.

Keywords: CT · metal artifact reduction · multi-perspective regularizations · iterative learning · wavelet transform

1 Introduction

Metal artifact could significantly affect the clinical diagnoses with computed tomography (CT) images, and how to effectively reduce it is a critical but challenging issue. Specifically, metal artifact is caused by metallic implants and often exhibits as bright and dark streaks in the reconstructed images [7]. These streaks could hinder the perception of the actual contents, posing a serious obstacle for radiologists in making an accurate diagnosis [26]. Making matters worse, with the increasing employment of metallic implants, metal artifacts in CT images have become more widespread. In this case, effectively reducing metal artifacts while maintaining the tissue details is of great clinical significance [20].

Since the metal artifacts are structured and non-local, they are tough to be removed from images directly [8]. Most of the traditional methods propose to reduce metal artifacts in the sinogram domain [6, 13, 21]. For instance, linear interpolation (LI) [6] and normalization metal artifacts reduction (NMAR) [13] weakened metal artifacts by substituting metal trace regions with interpolated data. However, severe secondary artifacts are induced by interpolation errors. Another commonly used iterative reconstruction algorithm [12] is computationally expensive. Some other researchers also explore a combination of multiple traditional methods to leverage their advantages [5] and improve their performance.

In contrast to the traditional methods mentioned above, deep learning-based MAR methods are undergoing more intensive studies and become a dominant approach to MAR. Depending on the performing domain, they can be categorized into three types, i.e., sinogram domain-based, image domain-based, and dual-domain-based. Specifically, i). the sinogram domain-based methods leverage the advantage that the signals of metal artifacts are concentrated in form of metal trace(s) and can be easily separated from the informative image contents in the sinogram domain [3, 15, 17]. However, they are restricted by the availability of the physical scanning configurations, and slight disturbance in the sinogram could cause serious artifacts in the image domain; ii). the image domain-based methods directly reduce metal artifacts in the image domain by utilizing residual [22] or adversarial learning [10, 24, 25, 29] techniques. However, the deep intertwinement of artifacts and the image contents in the image domain makes them arduous to be differentiated, limiting the network performance; iii). the dual-domain-based methods utilize both the sinogram and image domains to reduce metal artifacts [8, 28]. They typically involve alternative reduction of metal artifacts in the sinogram domain and refinement of image contents in the image domain, e.g., dual-domain data consistent recurrent network [32] and deep unrolling dual-domain network [23]. However, they cannot completely resolve the problem of secondary artifact and still require physical scanning configurations. In addition, most of the three above types of deep learning-based methods lack interpretability since they perform MAR in a black-box mechanism.

To address the issues of the existing methods aforementioned, we propose a Multi-perspective Adaptive Iteration Network(MAIN), and our main contributions are as follows:

- 1) **Multi-perspective Regularizations:** Based on the insightful analysis on the limitations of using sinograms in MAR, this paper innovatively identifies that the desirable properties of wavelet transform could well address the issues of sinograms in MAR. i.e., the spatial distribution characteristics of metal artifacts under different domains and resolutions. Based on this, we integrate multi-domain, multi-frequency band, and multi-constraint into our scheme by exploiting wavelet transform. Therefore, we explicitly formulate such knowledge as a multi-perspective optimization model as shown in Fig. 1.
- 2) **Iterative Optimization Algorithm:** To solve the multi-perspective optimization model, we develop an iterative algorithm with the proximal gradient

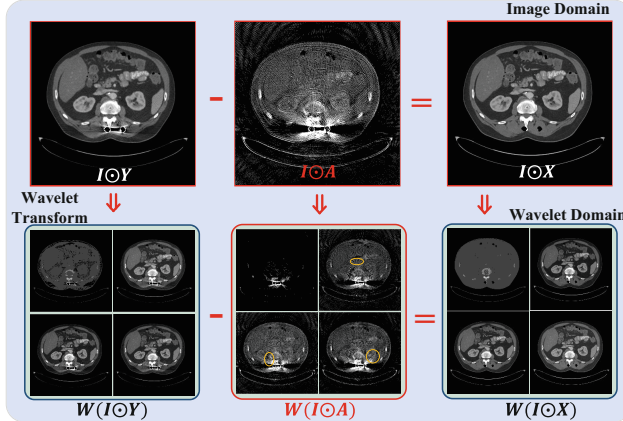


Fig. 1. The different distributions of metal artifacts. Here, Y , X , A and I denote the metal-corrupted CT image, clean CT image, metal artifacts and binary non-metal mask, respectively; \odot is the element-wise multiplication; and W denotes the adaptive wavelet transform.

technique [1]. The network is designed according to the algorithm to keep it in accordance with the procedure of the theoretical MAR optimization, making the network more interpretable.

- 3) **Adaptive Wavelet Transform:** In order to increase the flexibility and adaptivity of the proposed model, the proposed model conducts wavelet transforms with neural technology rather than the traditional fixed wavelet transform.

2 Method

Mathematical Model. In the image domain, it is easy to segment metal regions with much higher CT values [22]. As the metal regions have no human tissues, the clean CT image X can be defined as:

$$I \odot X = I \odot Y - I \odot A, \quad (1)$$

where $Y \in \mathbf{R}^{H \times W}$ is a metal-corrupted image, A and I denote the metal artifact and binary non-metal mask, respectively. \odot is the element-wise multiplication. To obtain a promising solution, various regularization terms representing prior constraints are introduced as:

$$\begin{aligned} \{X, A\} = \arg \min_{\{X, A\}} & \left\{ \frac{1}{2} \|I \odot (X + A - Y)\|_F^2 + \lambda_1 f_1(W(I \odot A)) \right. \\ & \left. + \lambda_2 f_2(W(I \odot X)) + \lambda_3 f_3(I \odot X) \right\} \end{aligned} \quad (2)$$

where W denotes the wavelet transform, $f_1(\cdot)$, $f_2(\cdot)$ and $f_3(\cdot)$ are regularization functions, and λ_1 , λ_2 and λ_3 are regularization weights. Specifically, $f_1(\cdot)$ and

$f_2(\cdot)$ represent wavelet domain constraints of X and A respectively, and $f_3(\cdot)$ introduces prior knowledge of X in the image domain. ε is an arbitrarily small number, and $\|\cdot\|_F^2$ is the Frobenius norm.

When the wavelet components are transformed back to the image domain, the image will be blurred due to information loss. To recover a more precise image, let $U = I \odot X'$ and introduce an error feedback item [14] into Eq. (2), where X' represents the CT image in the image domain obtained after performing inverse wavelet transform. Then, the optimization problem becomes:

$$\{X, A, U\} = \arg \min_{\{X, A, U\}} \left\{ \frac{1}{2} \|I \odot (X + A - Y)\|_F^2 + \frac{\beta}{2} \|I \odot X - U\|_F^2 + \lambda_1 f_1(W(I \odot A)) + \lambda_2 f_2(W(I \odot X)) + \lambda_3 f_3(U) \right\}, \quad (3)$$

where β is an adaptive weight.

Optimization Algorithm. In this paper, an alternating minimization strategy is used to solve Eq. (3). At the $(k+1)^{th}$ iteration, $A^{(k+1)}$, $X^{(k+1)}$ and $U^{(k+1)}$ are derived as the following three sub-problems:

$$\begin{cases} A^{(k+1)} = \arg \min_A \left\{ \frac{1}{2} \|I \odot (X^{(k)} + A - Y)\|_F^2 + \lambda_1 f_1(W(I \odot A)) \right\}, \\ X^{(k+1)} = \arg \min_X \left\{ \frac{1}{2} \|I \odot (X + A^{(k+1)} - Y)\|_F^2 + \frac{\beta}{2} \|I \odot X - U^{(k)}\|_F^2 + \lambda_2 f_2(W(I \odot X)) \right\}, \\ U^{(k+1)} = \arg \min_U \left\{ \frac{\beta}{2} \|(I \odot X^{(k+1)} - U)\|_F^2 \right\} + \lambda_3 f_3(U). \end{cases} \quad (4)$$

The Proximal Gradient Descent algorithm(PGD) [1] is applied to solve each sub-problems above. Taking the first sub-problem as an example, the Taylor formula is utilized to introduce $A^{(k)}$ into the approximation of $A^{(k+1)}$. Taylor's second-order expansion can be expressed as $f(x) = \frac{f''(x_0)}{2!}(x - x_0)^2 + f'(x_0)(x - x_0) + f(x_0) + o^n$. Let $g(A) = \|I \odot (X^{(k)} + A - Y)\|_F^2$. At $A = A^{(k)}$, the quadratic approximation of $A^{(k+1)}$ can be expressed as:

$$\begin{aligned} A^{(k+1)} = \arg \min_A & \left\{ \frac{\nabla^2 g(A^{(k)})}{2} \|I \odot (A - A^{(k)})\|_F^2 + g(A^{(k)}) + o(A) \right. \\ & \left. + \nabla g(A^{(k)})(I \odot (A - A^{(k)})) + 2\lambda_1 f_1(W(I \odot A)) \right\} \end{aligned} \quad (5)$$

Assuming that $\nabla^2 g(A^{(k)})$ is a non-zero constant that is replaced by $\frac{1}{\eta_1}$. Besides, $g(A^{(k)})$ is replaced by another constant $(\eta_1 \nabla g(A^{(k)}))^2$ to form a perfect square trinomial since changing constant does not affect the minimization of our objective function. Therefore, Eq. (5) is reformatted as

$$A^{(k+1)} = \arg \min_A \left\{ \frac{1}{2\eta_1} \|I \odot A - I \odot A^{(k)} + \eta_1 \nabla g(A^{(k)})\|_F^2 + 2\lambda_1 f_1(W(I \odot A)) \right\}, \quad (6)$$

In code implementation, a trainable parameter is used to represent η_1 . It is excepted that the application of adaptive parameter can assist network fitting A more preferably. In order to reveal the iterative procedure more apparently, an intermediate variable $A^{(k+0.5)}$ is introduced:

$$\begin{aligned} A^{(k+0.5)} &= I \odot A^{(k)} - \eta_1 \nabla g(A^{(k)}) \\ &= (1 - 2\eta_1)I \odot A^{(k)} + 2\eta_1 I \odot (Y - X^{(k)}). \end{aligned} \quad (7)$$

Based on the above derivations, an iteration equation can be formulated as [22]:

$$A^{(k+1)} = W^T prox_{\eta_1}(WA^{(k+0.5)}), \quad (8)$$

where $prox_{\eta_1}$ is the proximal operator [22] related to $f_1(\cdot)$. Since $f_1(\cdot)$ denotes the constraint on metal artifacts in wavelet domain, the iterative solution of A is carried out in wavelet domain. Since we eventually want to obtain artifacts in the image domain, W^T transforms the artifacts from wavelet domain to image domain. Similarly, $X^{(k+1)}$ and $U^{(k+1)}$ are derived as:

$$\begin{cases} X^{(k+1)} = W^T prox_{\eta_2}(WX^{(k+0.5)}), \\ U^{(k+1)} = prox_{\eta_3}(U^{(k+0.5)}). \end{cases} \quad (9)$$

where $prox_{\eta_2}$ and $prox_{\eta_3}$ are the proximal operator related to $f_2(\cdot)$ and $f_3(\cdot)$ respectively.

Network Design. Figure 2 depicts the flowchart of the proposed MAIN network. The network contains T iteration blocks. Following the optimization algorithm, each block contains three key modules of $proxNet_A$, $proxNet_X$ and $proxNet_U$. The three network modules are designed under the guidance of Eqs. (8) and (9) to respectively emulate the proximal operators of $prox_{\eta_1}$, $prox_{\eta_2}$ and $prox_{\eta_3}$.

At the $(k+1)^{th}$ block, $A^{(k)}$, $X^{(k)}$ and $U^{(k)}$ are first decomposed by adaptive wavelet transform module [18]. In the wavelet domain, the $proxNet_A$ and $proxNet_X$ are built by following the DnCNN [30], subsequently, $A^{(k+1)}$ and $X^{(k+1)}$ are computed. Next, $A^{(k+1)}$ and $X^{(k+1)}$ are converted to the image domain. And a lightweight U-Net [14, 19] is employed as $proxNet_U$.

3 Experiments

Synthetic Data. A synthetic dataset is generated by following the simulation procedure in [31]. Specifically, 1,200 clean CT images from Deeplesion [27] and 100 metal masks are collected for image synthesis. For network training, 1,000 CT images and 90 metal masks are randomly selected, creating 90,000 unique combinations. An additional 2,000 images are synthesized for test using the remaining 200 CT images and 10 metal masks. The pixel sizes of the 10 test masks are: 2054, 879, 878, 448, 242, 115, 115, 53, and 32.

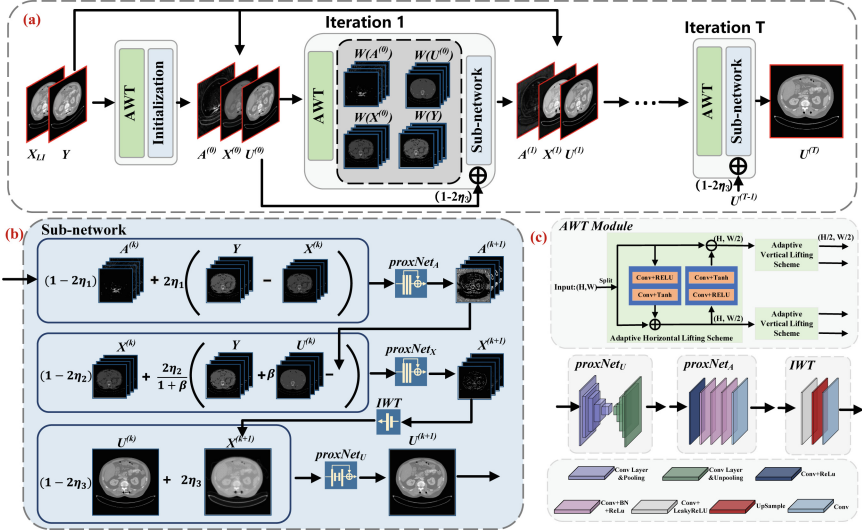


Fig. 2. The architecture of MAIN. (a) The overall architecture of our network with T iterations. (b) The procedure of sub-network at k^{th} iteration. (c) The detailed structure of adaptive wavelet transform and different proximal operator.

Clinical Data. In addition to the above synthetic data, the proposed model is also evaluated on the publicly available clinical dataset CLINIC-metal [9]. To keep consistent with Yu *et al.* [28], we segment the metal masks using a threshold of 2,000 HU. Then, the linear interpolated image is computed with the same procedure as synthetic data.

Implementation Details. The MAIN network is implemented using PyTorch [16] and trained with a single NVIDIA A6000 GPU for 120 epochs. We use the Adam optimizer with parameters $(\beta_1, \beta_2) = (0.5, 0.999)$, a learning rate of $5e^{-5}$, and a batch size of 16 to train the network. To enhance the stability of the model training, various image augmentations, such as image rotation and transposition, are applied.

Baseline and Evaluation Metric. Six state-of-the-art methods for metal artifact reduction are compared, including traditional method (NMAR [13]) and deep learning-based approaches (ACDNet [22], DuDoNet++ [11], DuDoNet [8] and CNNMAR [31]). DuDoNet and DuDoNet++ are reimplemented strictly adhering to the original methodology since they lacked open-source code. The Root Mean Square Error (RMSE) and Structural Similarity Index (SSIM) are used for quantitative assessment on the synthetic dataset. As reference images are unavailable on the clinical dataset, only visual comparison is conducted in terms of metal artifact reduction.

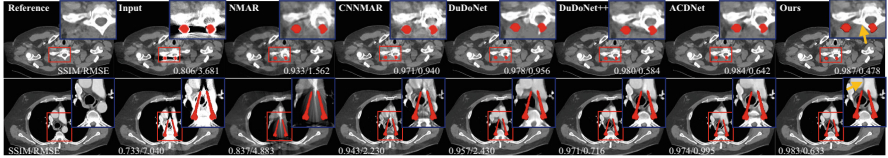


Fig. 3. Visual comparisons of MAR results on synthetic images. The display window is $[-224\ 634]$ HU.

Table 1. Quantitative comparison on synthetic testing dataset

Methods	NMAR	CNNMAR	DuDoNet	DuDoNet++	ACDNet	Ours
SSIM	0.910 ± 0.03	0.962 ± 0.02	0.974 ± 0.01	0.974 ± 0.01	0.980 ± 0.01	0.984 ± 0.01
RMSE	2.671 ± 0.82	1.077 ± 0.44	1.032 ± 0.41	0.716 ± 0.30	0.680 ± 0.21	0.628 ± 0.26

4 Results

Experimental Results on Synthetic Data. The visual comparison between our MAIN and other methods are shown in Fig. 3. Traditional method NMAR suffers from severe secondary artifacts due to interpolation errors, leading to blurred detailed structures. Although deep learning-based methods gets better results, the detailed structures around the metals are still blamed. In contrast to the above methods, our MAIN achieves the best result in metal artifact reduction and detail restoration. Table 1 presents the quantitative evaluation results of different methods, demonstrating that the MAIL network achieves the best performance with the highest values of SSIM (0.984) and RMSE (0.628).

Moreover, Fig. 4(a) displays the statistical results of different methods on the test set. Figure 4(b) shows the noise power spectrum (NPS) maps [2]. Figure 4(c) shows the intensity profiles [4] of different MAR results. These results demonstrate that the proposed method is highly stable and effective in dealing with different metallic implants.

Experimental Results on Clinical Data. Figure 5 shows the visual comparison on a clinical CT image with metal artifacts. It can be observed that the secondary artifacts caused by NMAR are severe, and other baselines would blur the tissue near the metallic implants. In comparison, our MAIN has achieved the best results in reducing metal artifacts and recovering tissue details.

Ablation Studies. We re-configure our network and retrain the model in image domain and wavelet domain, respectively. We also utilize ‘db3’ wavelet to re-configure the network and compare the corresponding model with the adaptive wavelet. It can be observed from Fig. 6 and Table 2 that our approach for reducing metal artifacts in both the wavelet and image domains is more effective than the single domain scheme. Moreover, the effectiveness of the adaptive wavelet transform is also confirmed.

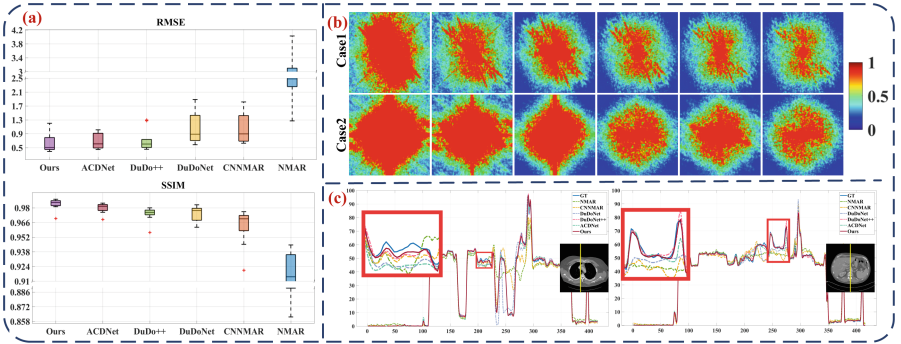


Fig. 4. (a) Visualization of statistical results on 2000 testing data. (b) NPS maps of MAR in cases 1 and 2. The 1st - 6th columns denote NMAR, CNNMAR, DuDoNet, DuDoNet++, ACDNet and our method. (c) The intensity profiles along the specified yellow line. (Color figure online)

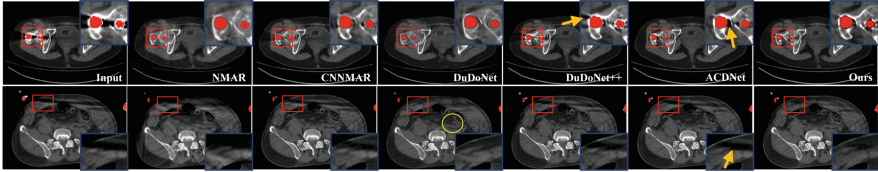


Fig. 5. Visual comparisons of MAR results on clinical images. The display window is $[-142 \text{ } 532]$ HU.

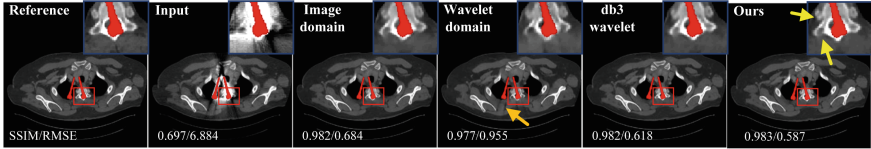


Fig. 6. Effectiveness verification of dual-domain and adaptive wavelet scheme.

Table 2. Quantitative analysis results of our methods on synthetic dataset

Method	wavelet domain	image domain	normal wavelet	ours
SSIM	0.978 ± 0.009	0.983 ± 0.005	0.983 ± 0.006	0.984 ± 0.005
RMSE	0.823 ± 0.345	0.664 ± 0.271	0.663 ± 0.307	0.628 ± 0.263

5 Discussion and Conclusion

In this study, we propose a multi-perspective adaptive iteration learning network for metal artifact reduction. The multi-perspective regularizations introduces prior knowledge in wavelet and image domain to constrain the feasible region

of the solution space. The employment of adaptive wavelet transform makes full use of the powerful learning ability of data-driven model, and it enhances the flexibility of the model. The comprehensive experiments on both of a synthetic and a clinical datasets have consistently verified the effectiveness of our method.

Acknowledgements. This work was supported in part by National Natural Science Foundation of China (grant numbers 62101611 and 62201628), National Key Research and Development Program of China (2022YFA1204200), Guangdong Basic and Applied Basic Research Foundation (grant number 2022A1515011375, 2023A1515012278, 2023A1515011780) and Shenzhen Science and Technology Program (grant number JCYJ20220530145411027, JCYJ20220818102414031).

References

1. Beck, A., Teboulle, M.: A fast iterative Shrinkage-Thresholding algorithm for linear inverse problems. *SIAM J. Imaging Sci.* **2**(1), 183–202 (2009)
2. Diwakar, M., Kumar, M.: A review on CT image noise and its denoising. *Biomed. Signal Process. Control* **42**, 73–88 (2018)
3. Ghani, M.U., Karl, W.: Deep learning based sinogram correction for metal artifact reduction. *Electron. Imaging* **2018**, 4721–4728 (2018)
4. Ghose, S., Singh, N., Singh, P.: Image denoising using deep learning: convolutional neural network. In: 2020 10th International Conference on Cloud Computing, Data Science & Engineering (Confluence), pp. 511–517 (2020)
5. Gjesteby, L., et al.: Metal artifact reduction in CT: where are we after four decades? *IEEE Access* **4**, 5826–5849 (2016)
6. Kalender, W.A., Hebel, R., Ebersberger, J.: Reduction of CT artifacts caused by metallic implants. *Radiology* **164**(2), 576–577 (1987)
7. Katsura, M., Sato, J., Akahane, M., Kunimatsu, A., Abe, O.: Current and novel techniques for metal artifact reduction at CT: practical guide for radiologists. *Radiographics* **38**(2), 450–461 (2018)
8. Lin, W.A., et al.: DuDoNet: dual domain network for CT metal artifact reduction. In: Proceedings of the IEEE/CVF Conference on Computer Vision and Pattern Recognition (CVPR) (2019)
9. Liu, P., et al.: Deep learning to segment pelvic bones: large-scale CT datasets and baseline models. *Int. J. Comput. Assist. Radiol. Surg.* **16**(5), 749–756 (2021). <https://doi.org/10.1007/s11548-021-02363-8>
10. Luo, Y., et al.: Adaptive rectification based adversarial network with spectrum constraint for high-quality PET image synthesis. *Med. Image Anal.* **77**, 102335 (2022)
11. Lyu, Y., Lin, W.-A., Liao, H., Lu, J., Zhou, S.K.: Encoding metal mask projection for metal artifact reduction in computed tomography. In: Martel, A.L., et al. (eds.) MICCAI 2020. LNCS, vol. 12262, pp. 147–157. Springer, Cham (2020). https://doi.org/10.1007/978-3-030-59713-9_15
12. Medoff, B.P., Brody, W.R., Nassi, M., Macovski, A.: Iterative convolution back-projection algorithms for image reconstruction from limited data. *J. Opt. Soc. Am.* **73**(11), 1493–1500 (1983)
13. Meyer, E., Raupach, R., Lell, M., Schmidt, B., Kachelrieß, M.: Normalized metal artifact reduction (NMAR) in computed tomography. *Med. Phys.* **37**(10), 5482–5493 (2010)

14. Pan, J., Zhang, H., Wu, W., Gao, Z., Wu, W.: Multi-domain integrative swin transformer network for sparse-view tomographic reconstruction. *Patterns* **3**(6), 100498 (2022)
15. Park, H.S., Lee, S.M., Kim, H.P., Seo, J.K., Chung, Y.E.: CT sinogram-consistency learning for metal-induced beam hardening correction. *Med. Phys.* **45**(12), 5376–5384 (2018)
16. Paszke, A., et al.: Automatic differentiation in PyTorch (2017)
17. Peng, C., et al.: An irregular metal trace inpainting network for X-ray CT metal artifact reduction. *Med. Phys.* **47**(9), 4087–4100 (2020)
18. Rodriguez, M.X.B., et al.: Deep adaptive wavelet network. In: Proceedings of the IEEE/CVF Winter Conference on Applications of Computer Vision (WACV) (2020)
19. Ronneberger, O., Fischer, P., Brox, T.: U-Net: convolutional networks for biomedical image segmentation. In: Navab, N., Hornegger, J., Wells, W.M., Frangi, A.F. (eds.) MICCAI 2015. LNCS, vol. 9351, pp. 234–241. Springer, Cham (2015). https://doi.org/10.1007/978-3-319-24574-4_28
20. Rousselle, A., et al.: Metallic implants and CT artefacts in the CTV area: where are we in 2020? *Cancer/Radiothérapie* **24**(6), 658–666 (2020). 31e Congrès national de la Société française de radiothérapie oncologique
21. Verburg, J.M., Seco, J.: CT metal artifact reduction method correcting for beam hardening and missing projections. *Phys. Med. Biol.* **57**(9), 2803 (2012)
22. Wang, H., Li, Y., Meng, D., Zheng, Y.: Adaptive convolutional dictionary network for CT metal artifact reduction. In: Raedt, L.D. (ed.) Proceedings of the Thirty-First International Joint Conference on Artificial Intelligence, IJCAI 2022, pp. 1401–1407. International Joint Conferences on Artificial Intelligence Organization (2022)
23. Wang, H., et al.: InDuDoNet: an interpretable dual domain network for CT metal artifact reduction. In: de Bruijne, M., et al. (eds.) MICCAI 2021. LNCS, vol. 12906, pp. 107–118. Springer, Cham (2021). https://doi.org/10.1007/978-3-030-87231-1_11
24. Wang, J., Zhao, Y., Noble, J.H., Dawant, B.M.: Conditional generative adversarial networks for metal artifact reduction in CT images of the ear. In: Frangi, A.F., Schnabel, J.A., Davatzikos, C., Alberola-López, C., Fichtinger, G. (eds.) MICCAI 2018. LNCS, vol. 11070, pp. 3–11. Springer, Cham (2018). https://doi.org/10.1007/978-3-030-00928-1_1
25. Wang, Y., et al.: 3D auto-context-based locality adaptive multi-modality GANs for PET synthesis. *IEEE Trans. Med. Imaging* **38**(6), 1328–1339 (2019)
26. Wellenberg, R., Hakvoort, E., Slump, C., Boomsma, M., Maas, M., Streekstra, G.: Metal artifact reduction techniques in musculoskeletal CT-imaging. *Eur. J. Radiol.* **107**, 60–69 (2018)
27. Yan, K., et al.: Deep lesion graphs in the wild: relationship learning and organization of significant radiology image findings in a diverse large-scale lesion database. In: Proceedings of the IEEE Conference on Computer Vision and Pattern Recognition (CVPR) (2018)
28. Yu, L., Zhang, Z., Li, X., Xing, L.: Deep sinogram completion with image prior for metal artifact reduction in CT images. *IEEE Trans. Med. Imaging* **40**(1), 228–238 (2021)
29. Zhan, B., et al.: Multi-constraint generative adversarial network for dose prediction in radiotherapy. *Med. Image Anal.* **77**, 102339 (2022)

30. Zhang, K., Zuo, W., Chen, Y., Meng, D., Zhang, L.: Beyond a Gaussian denoiser: residual learning of deep CNN for image denoising. *IEEE Trans. Image Process.* **26**(7), 3142–3155 (2017)
31. Zhang, Y., Yu, H.: Convolutional neural network based metal artifact reduction in X-ray computed tomography. *IEEE Trans. Med. Imaging* **37**(6), 1370–1381 (2018)
32. Zhou, B., Chen, X., Zhou, S.K., Duncan, J.S., Liu, C.: DuDoDR-Net: dual-domain data consistent recurrent network for simultaneous sparse view and metal artifact reduction in computed tomography. *Med. Image Anal.* **75**, 102289 (2022)